# Precision Measurement of the $(e^+ + e^-)$ Flux in Primary Cosmic Rays from 0.5 GeV to 1 TeV with the Alpha Magnetic Spectrometer on the International Space Station

M. Aguilar,[26] D. Aisa,[33,34] B. Alpat,[33] A. Alvino,[33] G. Ambrosi,[33] K. Andeen,[22] L. Arruda,[24] N. Attig,[21] P. Azzarello,[33,16,a] A. Bachlechner,[1] F. Barao,[24] A. Barrau,[17] L. Barrin,[15] A. Bartoloni,[38] L. Basara,[3,37] M. Battarbee,[44] R. Battiston,[37,b] J. Bazo,[33] U. Becker,[9] M. Behlmann,[9] B. Beischer,[1] J. Berdugo,[26] B. Bertucci,[33,34] G. Bigongiari,[35,36] V. Bindi,[19] S. Bizzaglia,[33] M. Bizzarri,[33,34] G. Boella,[28,29] W. de Boer,[22] K. Bollweg,[20] V. Bonnivard,[17] B. Borgia,[38,39] S. Borsini,[33] M. J. Boschini,[28] M. Bourquin,[16] J. Burger,[9] F. Cadoux,[16] X. D. Cai,[9] M. Capell,[9] S. Caroff,[3] J. Casaus,[26] V. Cascioli,[33] G. Castellini,[14] I. Cernuda,[26] F. Cervelli,[35] M. J. Chae,[40] Y. H. Chang,[10] A. I. Chen,[9] H. Chen,[9] G. M. Cheng,[6] H. S. Chen,[6] L. Cheng,[41] A. Chikanian,[32,*] H. Y. Chou,[10] E. Choumilov,[9] V. Choutko,[9] C. H. Chung,[1] C. Clark,[20] R. Clavero,[23] G. Coignet,[3] C. Consolandi,[19] A. Contin,[7,8] C. Corti,[19] B. Coste,[37] M. Crispoltoni,[33,34] Z. Cui,[41] M. Dai,[5] C. Delgado,[26] S. Della Torre,[28] M. B. Demirköz,[2] L. Derome,[17] S. Di Falco,[35] L. Di Masso,[33,34] F. Dimiccoli,[37] C. Díaz,[26] P. von Doetinchem,[19] F. Donnini,[33,34] W. J. Du,[41] M. Duranti,[33] D. D'Urso,[33] A. Eline,[9] F. J. Eppling,[9] T. Eronen,[44] Y. Y. Fan,[43,c] L. Farnesini,[33] J. Feng,[3,d] E. Fiandrini,[33,34] A. Fiasson,[3] E. Finch,[32] P. Fisher,[9] Y. Galaktionov,[9] G. Gallucci,[35,15] B. García,[26] R. García-López,[23] C. Gargiulo,[15] H. Gast,[1] I. Gebauer,[22] M. Gervasi,[28,29] A. Ghelfi,[17] W. Gillard,[10] F. Giovacchini,[26] P. Goglov,[9] J. Gong,[31] C. Goy,[3] V. Grabski,[27] D. Grandi,[28] M. Graziani,[33,15] C. Guandalini,[7,8] I. Guerri,[35,36] K. H. Guo,[18] M. Habiby,[16] S. Haino,[10,43] K. C. Han,[25] Z. H. He,[18] M. Heil,[9] J. Hoffman,[10] T. H. Hsieh,[9] Z. C. Huang,[18] C. Huh,[13] M. Incagli,[35] M. Ionica,[33] W. Y. Jang,[13] H. Jinchi,[25] K. Kanishev,[37] G. N. Kim,[13] K. S. Kim,[13] Th. Kirn,[1] R. Kossakowski,[3] O. Kounina,[9] A. Kounine,[9] V. Koutsenko,[9] M. S. Krafczyk,[9] S. Kunz,[22] G. La Vacca,[28,15] E. Laudi,[33,34,e] G. Laurenti,[7,8] I. Lazzizzera,[37] A. Lebedev,[9] H. T. Lee,[43] S. C. Lee,[43] C. Leluc,[16] H. L. Li,[43,f] J. Q. Li,[31] Q. Li,[31] Q. Li,[9,g] T. X. Li,[18] W. Li,[4] Y. Li,[16,d] Z. H. Li,[6] Z. Y. Li,[43,d] S. Lim,[40] C. H. Lin,[43] P. Lipari,[38] T. Lippert,[21] D. Liu,[43] H. Liu,[31] T. Lomtadze,[35] M. J. Lu,[37,h] Y. S. Lu,[6] K. Luebelsmeyer,[1] F. Luo,[41] J. Z. Luo,[31] S. S. Lv,[18] R. Majka,[32] A. Malinin,[12] C. Mañá,[26] J. Marín,[26] T. Martin,[20] G. Martínez,[26] N. Masi,[7,8] D. Maurin,[17] A. Menchaca-Rocha,[27] Q. Meng,[31] D. C. Mo,[18] L. Morescalchi,[35,i] P. Mott,[20] M. Müller,[1] J. Q. Ni,[18] N. Nikonov,[22] F. Nozzoli,[33] P. Nunes,[24] A. Obermeier,[1] A. Oliva,[26] M. Orcinha,[24] F. Palmonari,[7,8] C. Palomares,[26] M. Paniccia,[16] A. Papi,[33] M. Pauluzzi,[33,34] E. Pedreschi,[35] S. Pensotti,[28,29] R. Pereira,[24,19] F. Pilo,[35] A. Piluso,[33,34] C. Pizzolotto,[33] V. Plyaskin,[9] M. Pohl,[16] V. Poireau,[3] E. Postaci,[2] A. Putze,[3] L. Quadrani,[7,8] X. M. Qi,[18] T. Räihä,[1] P. G. Rancoita,[28] D. Rapin,[16] J. S. Ricol,[17] I. Rodríguez,[26] S. Rosier-Lees,[3] A. Rozhkov,[9] D. Rozza,[28] R. Sagdeev,[11] J. Sandweiss,[32] P. Saouter,[16] C. Sbarra,[7,8] S. Schael,[1] S. M. Schmidt,[21] D. Schuckardt,[22] A. Schulz von Dratzig,[1] G. Schwering,[1] G. Scolieri,[33] E. S. Seo,[12] B. S. Shan,[4] Y. H. Shan,[4] J. Y. Shi,[31] X. Y. Shi,[9,j] Y. M. Shi,[42] T. Siedenburg,[1] D. Son,[13] F. Spada,[38] F. Spinella,[35] W. Sun,[9] W. H. Sun,[9,k] M. Tacconi,[28,29] C. P. Tang,[18] X. W. Tang,[6] Z. C. Tang,[6] L. Tao,[3] D. Tescaro,[23] Samuel C. C. Ting,[9] S. M. Ting,[9] N. Tomassetti,[17] J. Torsti,[44] C. Türkoğlu,[2] T. Urban,[20] V. Vagelli,[22] E. Valente,[38,39] C. Vannini,[35] E. Valtonen,[44] S. Vaurynovich,[9] M. Vecchi,[3] M. Velasco,[26] J. P. Vialle,[3] L. Q. Wang,[41] Q. L. Wang,[5] R. S. Wang,[42] X. Wang,[9] Z. X. Wang,[18] Z. L. Weng,[9] K. Whitman,[19] J. Wienkenhöver,[1] H. Wu,[31] X. Xia,[26,f] M. Xie,[9,g] S. Xie,[42] R. Q. Xiong,[31] G. M. Xin,[41] N. S. Xu,[18] W. Xu,[6,9] Q. Yan,[6] J. Yang,[40] M. Yang,[6] Q. H. Ye,[42] H. Yi,[31] Y. J. Yu,[5] Z. Q. Yu,[6] S. Zeissler,[22] J. H. Zhang,[31] M. T. Zhang,[18] X. B. Zhang,[18] Z. Zhang,[18] Z. M. Zheng,[4] H. L. Zhuang,[6] V. Zhukov,[1] A. Zichichi,[7,8] N. Zimmermann,[1] P. Zuccon,[9] C. Zurbach[30]

(AMS Collaboration)

[1]*I. Physics Institute and JARA-FAME, RWTH Aachen University, D–52056 Aachen, Germany*
[2]*Department of Physics, Middle East Technical University (METU), 06800 Ankara, Turkey*
[3]*Laboratoire d'Annecy–Le–Vieux de Physique des Particules (LAPP), IN2P3/CNRS and Université de Savoie, F–74941 Annecy–le–Vieux, France*
[4]*Beihang University (BUAA), Beijing 100191, China*
[5]*Institute of Electrical Engineering (IEE), Chinese Academy of Sciences, Beijing 100080, China*
[6]*Institute of High Energy Physics (IHEP), Chinese Academy of Sciences, Beijing 100039, China*
[7]*INFN Sezione di Bologna, I–40126 Bologna, Italy*
[8]*Università di Bologna, I–40126 Bologna, Italy*
[9]*Massachusetts Institute of Technology (MIT), Cambridge, Massachusetts 02139, USA*
[10]*National Central University (NCU), Chung–Li, Tao Yuan 32054, Taiwan*
[11]*East–West Center for Space Science, University of Maryland, College Park, Maryland 20742, USA*
[12]*IPST, University of Maryland, College Park, Maryland 20742, USA*

 

[13]CHEP, Kyungpook National University, 702–701 Daegu, Korea
[14]CNR–IROE, I-50125 Firenze, Italy
[15]European Organization for Nuclear Research (CERN), CH–1211 Geneva 23, Switzerland
[16]DPNC, Université de Genève, CH–1211 Genève 4, Switzerland
[17]Laboratoire de Physique Subatomique et de Cosmologie (LPSC), CNRS/IN2P3 and Université Grenoble–Alpes, F–38026 Grenoble, France
[18]Sun Yat–Sen University (SYSU), Guangzhou 510275, China
[19]Physics and Astronomy Department, University of Hawaii, 2505 Correa Road, WAT 432, Honolulu, Hawaii 96822, USA
[20]National Aeronautics and Space Administration Johnson Space Center (JSC), and Jacobs-Sverdrup, Houston, Texas 77058, USA
[21]Jülich Supercomputing Centre and JARA-FAME, Research Centre Jülich, D–52425 Jülich, Germany
[22]Institut für Experimentelle Kernphysik, Karlsruhe Institute of Technology (KIT), D–76128 Karlsruhe, Germany
[23]Instituto de Astrofísica de Canarias (IAC), E–38205 La Laguna, Tenerife, Spain
[24]Laboratório de Instrumentação e Física Experimental de Partículas, (LIP), P–1000 Lisboa, Portugal
[25]National Chung–Shan Institute of Science and Technology (NCSIST), Longtan, Tao Yuan 325, Taiwan
[26]Centro de Investigaciones Energéticas, Medioambientales y Tecnológicas (CIEMAT), E–28040 Madrid, Spain
[27]Instituto de Física, Universidad Nacional Autónoma de México (UNAM), México D.F. 01000, Mexico
[28]INFN Sezione di Milano–Bicocca, I–20126 Milano, Italy
[29]Università di Milano–Bicocca, I–20126 Milano, Italy
[30]Laboratoire Univers et Particules de Montpellier (LUPM), IN2P3/CNRS and Université de Montpellier II, F–34095 Montpellier, France
[31]Southeast University (SEU), Nanjing 210096, China
[32]Physics Department, Yale University, New Haven, Connecticut 06520, USA
[33]INFN Sezione di Perugia, I–06100 Perugia, Italy
[34]Università di Perugia, I–06100 Perugia, Italy
[35]INFN Sezione di Pisa, I–56100 Pisa, Italy
[36]Università di Pisa, I–56100 Pisa, Italy
[37]INFN TIFPA and Università di Trento, I–38123 Povo, Trento, Italy
[38]INFN Sezione di Roma 1, I–00185 Roma, Italy
[39]Università di Roma La Sapienza, I–00185 Roma, Italy
[40]Department of Physics, Ewha Womans University, Seoul 120-750, Korea
[41]Shandong University (SDU), Jinan, Shandong 250100, China
[42]Shanghai Jiaotong University (SJTU), Shanghai 200030, China
[43]Institute of Physics, Academia Sinica, Nankang, Taipei 11529, Taiwan
[44]Space Research Laboratory, Department of Physics and Astronomy, University of Turku, FI–20014 Turku, Finland
(Received 5 September 2014; published 26 November 2014)

We present a measurement of the cosmic ray $(e^+ + e^-)$ flux in the range 0.5 GeV to 1 TeV based on the analysis of 10.6 million $(e^+ + e^-)$ events collected by AMS. The statistics and the resolution of AMS provide a precision measurement of the flux. The flux is smooth and reveals new and distinct information. Above 30.2 GeV, the flux can be described by a single power law with a spectral index $\gamma = -3.170 \pm 0.008(\text{stat} + \text{syst}) \pm 0.008(\text{energy scale})$.

DOI: 10.1103/PhysRevLett.113.221102 PACS numbers: 96.50.sb, 95.35.+d, 95.85.Ry, 98.70.Sa

Measurements of cosmic rays by the Alpha Magnetic Spectrometer (AMS) [1–3] of the positron fraction and the positron flux $\Phi(e^+)$ have been carried out up to 500 GeV and of the electron flux $\Phi(e^-)$ up to 700 GeV. The results generated widespread interest and discussions on the origin of high-energy positrons and electrons [4]. They provide information on the combined flux $\Phi(e^+ + e^-)$ up to 500 GeV. In this Letter we present a dedicated measurement of $\Phi(e^+ + e^-)$ up to 1 TeV with reduced statistical and systematic errors.

*AMS.*—AMS is a general purpose high-energy particle physics detector installed on the International Space Station (ISS) to conduct a unique long-duration (~20-yr) mission of fundamental physics research in space [5]. It consists of a tracker, a magnet, time of flight (TOF) and anticoincidence counters, a ring imaging Čerenkov detector, an electromagnetic calorimeter (ECAL), and a transition radiation detector (TRD).

The nine layer double-sided silicon microstrip tracker accurately determines the trajectory and absolute charge $|Z|$ of cosmic rays using multiple measurements of the coordinates and energy loss. Together with the 0.14 T permanent magnet, the tracker measures the particle rigidity $R = p/Z$, where $p$ is the momentum. The maximum detectable rigidity is 2 TV over a lever arm of 3 m.

The four TOF planes trigger the readout of all the detectors and measure the particle velocity and direction. The high efficiency (≃99.999%) anticoincidence counters

inside the magnet bore are used to reject particles outside the geometric acceptance. The tracker, TOF, and TRD measure $|Z|$ independently. The curvature measured with the tracker and the magnet and the direction of the particle measured with the TOF yield the sign of the charge.

The 3-dimensional imaging capability of the 17 radiation length ($17X_0$) ECAL allows for an accurate measurement of the $(e^+ + e^-)$ energy $E$ scaled to the top of AMS and of the shower shape. An ECAL estimator, based on a boosted decision tree algorithm [6], is used to differentiate $(e^+ + e^-)$ from protons by exploiting their different shower shapes.

To further differentiate between $(e^+ + e^-)$ and protons, signals from the 20 layers of proportional tubes in the TRD are combined into a TRD classifier formed from the product of the probabilities of the $(e^+ + e^-)$ hypothesis. This TRD classifier has the same differentiation power as the TRD likelihood variable used in [3] but has a different scale.

The timing, location, and attitude are determined by a combination of GPS units affixed to AMS and to the ISS. AMS operates continuously on the ISS and is monitored and controlled around the clock from the ground. The detector performance is steady over time.

The entire detector has been extensively calibrated in a test beam at CERN with $e^+$ and $e^-$ from 10 to 290 GeV/$c$, with protons at 180 and 400 GeV/$c$, and with $\pi^\pm$ from 10 to 180 GeV/$c$ which produce transition radiation equivalent to protons up to 1.2 TeV/$c$. Measurements with 18 different energies and particles at 2000 positions were performed. A Monte Carlo program based on the GEANT 4.9.4 package [7] is used to simulate physics processes and detector signals.

*Analysis.*—Over $41 \times 10^9$ events collected from May 19, 2011, to November 26, 2013, have been analyzed. The isotropic $(e^+ + e^-)$ flux is measured in each energy bin $E$, of width $\Delta E$, as

$$\Phi(e^+ + e^-) = \frac{N(E)}{A_{\rm eff}(E)\epsilon_{\rm trig}(E)\epsilon_{\rm ECAL}(E)T(E)\Delta E} \quad (1)$$

where $N$ is the number of $(e^+ + e^-)$ events, $A_{\rm eff}$ is the effective detector acceptance, $\epsilon_{\rm trig}$ is the trigger efficiency, $\epsilon_{\rm ECAL}$ is the signal selection efficiency based on the ECAL estimator, and $T$ is the exposure time.

Equation (1) is evaluated independently in 74 energy bins from 0.5 GeV to 1 TeV. The bin width is chosen to be at least two times the energy resolution. The bin-to-bin migration error is ~1% at 1 GeV decreasing to 0.2% above 10 GeV. With increasing energy the bin width smoothly increases to ensure adequate statistics in each bin.

The absolute energy scale is verified by using minimum ionizing particles and the ratio $E/p$. These results are compared with the test beam values where the beam energy is known to high precision. This comparison limits the uncertainty of the absolute energy scale to 2% in the range covered by the test beam results, 10–290 GeV. Below 10 GeV it increases to 5% at 0.5 GeV and above 290 GeV to 5% at 1 TeV. This is treated as an uncertainty on the bin boundaries.

Events are selected requiring the presence of a downward-going, $\beta > 0.83$ particle which has hits in at least 8 of the 20 TRD layers and a single track in the tracker passing through the ECAL. Events with an energy deposition compatible with a minimum ionizing particle in the first $5X_0$ of the ECAL are rejected. Events with $|Z| > 1$ are rejected using $dE/dx$ in the tracker and TRD. Secondary particles of atmospheric origin [8] are rejected with the cutoff requirement discussed below.

In each energy bin, TRD classifier reference spectra of the $(e^+ + e^-)$ signal and the proton background are used as templates. The templates are constructed from the data using pure samples of $e^-$ and protons. These samples are selected using the ECAL estimator, $E/p$ matching, and the charge sign. The templates are evaluated separately in each bin; however, the signal templates show no dependence on the energy above ~10 GeV. Therefore, all the $e^-$ selected in the range 15.1–83.4 GeV are taken as a unique signal template up to the highest energies.

The sum of the signal and background templates is fit to the data by varying their normalizations. This yields the number of signal $(e^+ + e^-)$ events $N$ and the number of background (proton) events. It also yields the statistical errors on $N$ and the number of background events. These errors yield the statistical error on the flux. Figure 1 presents the data, the fit, and the signal and background templates for one bin.

The effective detector acceptance is

$$A_{\rm eff} = A_{\rm geom}\epsilon_{\rm sel}(1 + \delta), \quad (2)$$

where $A_{\rm geom}$ is the geometric acceptance, $\epsilon_{\rm sel}$ is the event selection efficiency, and $\delta$ is a data-derived correction. The

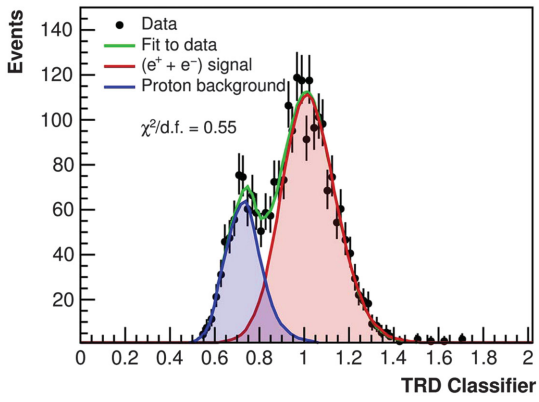


FIG. 1 (color). The result of the template fit in the 149–170 GeV bin showing the small proton background overlapping the $(e^+ + e^-)$ signal. The fit has a $\chi^2/d.f. = 0.55$.

acceptance for a particle that passes through the active volumes of the tracker, TRD, TOF, and ECAL is found to be $A_{\rm geom} \simeq 550$ cm$^2$ sr and $\epsilon_{\rm sel}$ has typical values of 90% at 10 GeV, 83% at 100 GeV, and 70% at 1 TeV. Both $A_{\rm geom}$ and $\epsilon_{\rm sel}$ are evaluated from the Monte Carlo simulation. The small correction to the acceptance $\delta$ is estimated by comparing the data and the Monte Carlo simulation efficiencies for every selection cut using information from the detectors unrelated to that cut. This correction is found to be a smooth, slowly varying function of energy. It is $-0.04$ at 2 GeV and $-0.03$ at 1 TeV.

The trigger efficiency is determined from data. The data acquisition system is triggered by the coincidence of all four TOF planes. AMS also records unbiased triggers which require a coincidence of any three out of the four TOF planes to measure $\epsilon_{\rm trig}$. It is 100% above 3 GeV decreasing to 75% at 1 GeV.

The ECAL estimator efficiency $\epsilon_{\rm ECAL}$ is measured from the data using negative rigidity samples and the selection cuts. $\epsilon_{\rm ECAL}$ values range from 75% to 95% for different energy bins, depending on the number of signal and background events.

The orbital parameters and the status of the detectors are recorded for each second of data-taking. Live-time weighted seconds are summed to obtain the exposure time in a given energy bin only when the minimum bin energy exceeds 1.2 times the maximum Størmer cutoff [9] for $|Z| = 1$ particles in the AMS geometric acceptance. The exposure time does not include time spent in the South Atlantic Anomaly, time during TRD gas refills, and time when the AMS $z$ axis was more than 40° from the local zenith. For the energy bins above ~30 GeV, where the effects of the geomagnetic cutoff are negligible, the exposure time is $6.2 \times 10^7$ seconds. It decreases to $1.5 \times 10^7$ seconds at 5 GeV.

A total of $10.6 \times 10^6$ $(e^+ + e^-)$ events have been identified with energies from 0.5 GeV to 1 TeV. A major experimental advantage of the combined flux analysis compared to the measurement of the individual positron and electron fluxes, particularly at high energies, is that the selection does not depend on the charge sign. Another advantage is that it has a higher overall efficiency. Consequently, this measurement is extended to 1 TeV with less overall uncertainty over the entire energy range. Systematic uncertainties arise from (i) the event selection, (ii) the acceptance, and (iii) bin-to-bin migration.

To evaluate the systematic uncertainty from the event selection which includes the uncertainty from the construction of the templates, 2000 trials were performed in each energy bin. Each trial consisted of the complete analysis. The trials were performed with different values of the ECAL estimator cut and different values of selection cuts used to construct the templates. The 2000 trials are performed in an interval of ±5% in efficiency around the value of the ECAL estimator cut which minimizes the

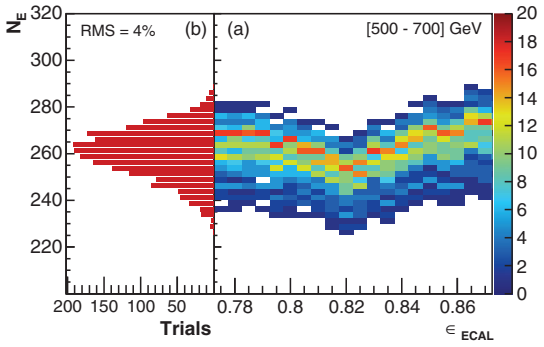


FIG. 2 (color). For the 500–700 GeV bin: (a) $N_E$ versus $\epsilon_{\rm ECAL}$ for the 2000 trials showing that the result is stable over a wide range of $\epsilon_{\rm ECAL}$. The scale on the right indicates the number of trials. (b) The distribution of $N_E$ for the 2000 trials. The narrow width (a rms of 4%) of the distribution indicates the accuracy at the highest energies.

combined statistical and systematic uncertainties. For the 500–700 GeV bin, Fig. 2(a) shows the stability of the number of signal events corrected by the ECAL estimator selection efficiency $N_E = N/\epsilon_{\rm ECAL}$ as a function of $\epsilon_{\rm ECAL}$. As seen, $N_E$ does not depend on the efficiency and this was found to be the case in every energy bin. Figure 2(b) shows the distribution of $N_E$ for the 2000 trials in this bin. The median value of the distribution determines the flux. The rms spread of the distribution provides an evaluation of the stability of the measurement. The difference between the width of this distribution in data and the expected statistical fluctuations quantifies the systematic uncertainty as $< 1\%$ below ~200 GeV increasing to 4% in the 500–700 GeV bin. This is the main source of systematic uncertainty above ~500 GeV.

The systematic error on the acceptance is given by the uncertainty on $\delta$. It is estimated from data to Monte Carlo simulation comparisons. Above 3 GeV a systematic error of 2% on $(1 + \delta)$ is obtained from the contributions of all the cuts. Below 3 GeV the uncertainty increases to 6% at 1 GeV. This is the major contribution to the systematic error below ~500 GeV. The systematic error on the acceptance includes a bin-to-bin correlation of 1.4% over the entire energy range.

*Results.*—The measured $(e^+ + e^-)$ flux is presented in Table I as a function of the energy at the top of AMS together with its statistical and systematic errors, where the systematic errors are the quadratic sum of the systematic uncertainties listed above, (i)-(iii). The table also contains a representative value of the energy in the bin, $\tilde{E}$, for a flux $\propto E^{-3}$ [10] and the error on $\tilde{E}$ according to the energy scale uncertainty. Several independent analyses were performed on the same data sample by different study groups. The results of those analyses are consistent with the results presented here. The flux multiplied by $\tilde{E}^3$ is presented in Fig. 3, together with previous measurements [11–17]. Below ~10 GeV, the behavior of $\Phi(e^+ + e^-)$ is affected

TABLE I. The electron plus positron flux $\Phi(e^+ + e^-)$ in units of $[\mathrm{GeV} \cdot \mathrm{m}^2 \cdot \mathrm{sr} \cdot \mathrm{s}]^{-1}$ with its statistical and systematic errors. The systematic uncertainties include an overall scaling uncertainty of 1.4% which introduces a correlation between bins. $\tilde{E}$ as described in the text with its systematic error derived from the energy scale uncertainty. The bin boundaries and $\tilde{E}$ are the energies at the top of AMS.

| Energy (GeV) | $\tilde{E}$ (GeV) | $\Phi(e^+ + e^-) \pm \sigma_{\mathrm{stat}} \pm \sigma_{\mathrm{syst}}$ |
|---|---|---|
| 0.50–0.65 | $0.57 \pm 0.03$ | $(2.71 \pm 0.10 \pm 0.54) \times 10^{+1}$ |
| 0.65–0.82 | $0.73 \pm 0.03$ | $(2.38 \pm 0.02 \pm 0.21) \times 10^{+1}$ |
| 0.82–1.01 | $0.91 \pm 0.04$ | $(2.17 \pm 0.01 \pm 0.16) \times 10^{+1}$ |
| 1.01–1.22 | $1.11 \pm 0.05$ | $(2.01 \pm 0.01 \pm 0.12) \times 10^{+1}$ |
| 1.22–1.46 | $1.33 \pm 0.05$ | $(1.78 \pm 0.01 \pm 0.09) \times 10^{+1}$ |
| 1.46–1.72 | $1.58 \pm 0.06$ | $(1.46 \pm 0.00 \pm 0.06) \times 10^{+1}$ |
| 1.72–2.00 | $1.85 \pm 0.07$ | $(1.19 \pm 0.00 \pm 0.04) \times 10^{+1}$ |
| 2.00–2.31 | $2.15 \pm 0.08$ | $(9.47 \pm 0.01 \pm 0.28) \times 10^{0}$ |
| 2.31–2.65 | $2.47 \pm 0.08$ | $(7.48 \pm 0.01 \pm 0.19) \times 10^{0}$ |
| 2.65–3.00 | $2.82 \pm 0.09$ | $(5.77 \pm 0.01 \pm 0.13) \times 10^{0}$ |
| 3.00–3.36 | $3.17 \pm 0.10$ | $(4.81 \pm 0.01 \pm 0.10) \times 10^{0}$ |
| 3.36–3.73 | $3.54 \pm 0.11$ | $(3.77 \pm 0.01 \pm 0.08) \times 10^{0}$ |
| 3.73–4.12 | $3.92 \pm 0.12$ | $(2.99 \pm 0.00 \pm 0.06) \times 10^{0}$ |
| 4.12–4.54 | $4.32 \pm 0.12$ | $(2.37 \pm 0.00 \pm 0.05) \times 10^{0}$ |
| 4.54–5.00 | $4.76 \pm 0.13$ | $(1.87 \pm 0.00 \pm 0.04) \times 10^{0}$ |
| 5.00–5.49 | $5.24 \pm 0.14$ | $(1.47 \pm 0.00 \pm 0.03) \times 10^{0}$ |
| 5.49–6.00 | $5.74 \pm 0.15$ | $(1.16 \pm 0.00 \pm 0.02) \times 10^{0}$ |
| 6.00–6.54 | $6.26 \pm 0.15$ | $(9.13 \pm 0.01 \pm 0.19) \times 10^{-1}$ |
| 6.54–7.10 | $6.81 \pm 0.16$ | $(7.24 \pm 0.01 \pm 0.15) \times 10^{-1}$ |
| 7.10–7.69 | $7.39 \pm 0.17$ | $(5.76 \pm 0.01 \pm 0.12) \times 10^{-1}$ |
| 7.69–8.30 | $7.99 \pm 0.18$ | $(4.57 \pm 0.01 \pm 0.09) \times 10^{-1}$ |
| 8.30–8.95 | $8.62 \pm 0.19$ | $(3.65 \pm 0.01 \pm 0.07) \times 10^{-1}$ |
| 8.95–9.62 | $9.28 \pm 0.19$ | $(2.92 \pm 0.01 \pm 0.06) \times 10^{-1}$ |
| 9.62–10.32 | $9.96 \pm 0.20$ | $(2.35 \pm 0.01 \pm 0.05) \times 10^{-1}$ |
| 10.3–11.0 | $10.7 \pm 0.2$ | $(1.89 \pm 0.00 \pm 0.04) \times 10^{-1}$ |
| 11.0–11.8 | $11.4 \pm 0.2$ | $(1.54 \pm 0.00 \pm 0.03) \times 10^{-1}$ |
| 11.8–12.6 | $12.2 \pm 0.2$ | $(1.26 \pm 0.00 \pm 0.03) \times 10^{-1}$ |
| 12.6–13.4 | $13.0 \pm 0.3$ | $(1.03 \pm 0.00 \pm 0.02) \times 10^{-1}$ |
| 13.4–14.2 | $13.8 \pm 0.3$ | $(8.42 \pm 0.03 \pm 0.17) \times 10^{-2}$ |
| 14.2–15.1 | $14.7 \pm 0.3$ | $(6.91 \pm 0.02 \pm 0.14) \times 10^{-2}$ |
| 15.1–16.1 | $15.6 \pm 0.3$ | $(5.73 \pm 0.02 \pm 0.12) \times 10^{-2}$ |
| 16.1–17.0 | $16.5 \pm 0.3$ | $(4.74 \pm 0.02 \pm 0.10) \times 10^{-2}$ |
| 17.0–18.0 | $17.5 \pm 0.3$ | $(3.93 \pm 0.02 \pm 0.08) \times 10^{-2}$ |
| 18.0–19.0 | $18.5 \pm 0.4$ | $(3.29 \pm 0.01 \pm 0.07) \times 10^{-2}$ |
| 19.0–20.0 | $19.5 \pm 0.4$ | $(2.75 \pm 0.01 \pm 0.06) \times 10^{-2}$ |
| 20.0–21.1 | $20.6 \pm 0.4$ | $(2.31 \pm 0.01 \pm 0.05) \times 10^{-2}$ |
| 21.1–22.2 | $21.7 \pm 0.4$ | $(1.94 \pm 0.01 \pm 0.04) \times 10^{-2}$ |
| 22.2–23.4 | $22.8 \pm 0.5$ | $(1.65 \pm 0.01 \pm 0.03) \times 10^{-2}$ |
| 23.4–24.6 | $24.0 \pm 0.5$ | $(1.39 \pm 0.01 \pm 0.03) \times 10^{-2}$ |
| 24.6–25.9 | $25.2 \pm 0.5$ | $(1.19 \pm 0.01 \pm 0.02) \times 10^{-2}$ |
| 25.9–27.2 | $26.6 \pm 0.5$ | $(9.98 \pm 0.06 \pm 0.20) \times 10^{-3}$ |
| 27.2–28.7 | $28.0 \pm 0.6$ | $(8.52 \pm 0.05 \pm 0.17) \times 10^{-3}$ |
| 28.7–30.2 | $29.4 \pm 0.6$ | $(7.22 \pm 0.04 \pm 0.15) \times 10^{-3}$ |
| 30.2–31.8 | $31.0 \pm 0.6$ | $(6.03 \pm 0.04 \pm 0.12) \times 10^{-3}$ |
| 31.8–33.5 | $32.7 \pm 0.7$ | $(5.15 \pm 0.03 \pm 0.11) \times 10^{-3}$ |
| 33.5–35.4 | $34.4 \pm 0.7$ | $(4.29 \pm 0.03 \pm 0.09) \times 10^{-3}$ |
| 35.4–37.3 | $36.3 \pm 0.7$ | $(3.64 \pm 0.03 \pm 0.07) \times 10^{-3}$ |
| 37.3–39.4 | $38.3 \pm 0.8$ | $(3.11 \pm 0.02 \pm 0.06) \times 10^{-3}$ |
| 39.4–41.6 | $40.5 \pm 0.8$ | $(2.59 \pm 0.02 \pm 0.05) \times 10^{-3}$ |
| 41.6–44.0 | $42.8 \pm 0.9$ | $(2.18 \pm 0.02 \pm 0.04) \times 10^{-3}$ |
| 44.0–46.6 | $45.3 \pm 0.9$ | $(1.81 \pm 0.02 \pm 0.04) \times 10^{-3}$ |
| 46.6–49.3 | $47.9 \pm 1.0$ | $(1.49 \pm 0.01 \pm 0.03) \times 10^{-3}$ |
| 49.3–52.3 | $50.8 \pm 1.0$ | $(1.24 \pm 0.01 \pm 0.03) \times 10^{-3}$ |
| 52.3–55.6 | $53.9 \pm 1.1$ | $(1.04 \pm 0.01 \pm 0.02) \times 10^{-3}$ |
| 55.6–59.1 | $57.3 \pm 1.1$ | $(8.62 \pm 0.10 \pm 0.18) \times 10^{-4}$ |
| 59.1–63.0 | $61.0 \pm 1.2$ | $(7.06 \pm 0.09 \pm 0.15) \times 10^{-4}$ |
| 63.0–67.3 | $65.1 \pm 1.3$ | $(5.62 \pm 0.07 \pm 0.12) \times 10^{-4}$ |
| 67.3–72.0 | $69.6 \pm 1.4$ | $(4.56 \pm 0.06 \pm 0.09) \times 10^{-4}$ |
| 72.0–77.4 | $74.6 \pm 1.5$ | $(3.66 \pm 0.05 \pm 0.08) \times 10^{-4}$ |
| 77.4–83.4 | $80.3 \pm 1.6$ | $(2.91 \pm 0.04 \pm 0.06) \times 10^{-4}$ |
| 83.4–90.2 | $86.7 \pm 1.7$ | $(2.32 \pm 0.04 \pm 0.05) \times 10^{-4}$ |
| 90.2–98.1 | $94.0 \pm 1.9$ | $(1.78 \pm 0.03 \pm 0.04) \times 10^{-4}$ |
| 98–107 | $103 \pm 2$ | $(1.37 \pm 0.03 \pm 0.03) \times 10^{-4}$ |
| 107–118 | $113 \pm 2$ | $(1.01 \pm 0.02 \pm 0.02) \times 10^{-4}$ |
| 118–132 | $125 \pm 3$ | $(7.26 \pm 0.15 \pm 0.15) \times 10^{-5}$ |
| 132–149 | $140 \pm 3$ | $(5.04 \pm 0.12 \pm 0.11) \times 10^{-5}$ |
| 149–170 | $159 \pm 3$ | $(3.55 \pm 0.09 \pm 0.08) \times 10^{-5}$ |
| 170–198 | $183 \pm 4$ | $(2.17 \pm 0.06 \pm 0.05) \times 10^{-5}$ |
| 198–237 | $216 \pm 4$ | $(1.27 \pm 0.04 \pm 0.03) \times 10^{-5}$ |
| 237–290 | $262 \pm 5$ | $(6.89 \pm 0.27 \pm 0.16) \times 10^{-6}$ |
| 290–370 | $327 \pm 7$ | $(3.45 \pm 0.17 \pm 0.09) \times 10^{-6}$ |
| 370–500 | $429 \pm 13$ | $(1.45 \pm 0.10 \pm 0.04) \times 10^{-6}$ |
| 500–700 | $589 \pm 22$ | $(5.41 \pm 0.56 \pm 0.23) \times 10^{-7}$ |
| 700–1000 | $832 \pm 38$ | $(1.90 \pm 0.40 \pm 0.23) \times 10^{-7}$ |

by solar modulation. However, above 20 GeV the effects of solar modulation are insignificant within the current experimental accuracy. The data show no structures. In particular, from 10 GeV to 1 TeV the flux is smooth and reveals new and distinct information.

As seen in Fig. 3, the flux cannot be described by a single power law ($\Phi \propto E^{\gamma}$) over the entire range. To estimate a lower energy limit above which a single power law describes the flux, we use energy intervals with starting energies from 0.5 GeV and increasing bin by bin. The ending energy for all intervals is fixed at 1 TeV. Each interval is split into two sections with a boundary between the starting energy and 1 TeV. Each of the two sections is fit with a single power law and we obtain two spectral indices. The lowest starting energy of the interval that gives consistent spectral indices at the 90% C.L. for any boundary yields a lower limit of 30.2 GeV.

To quantitatively examine the energy dependence of the flux in a model independent way, the flux is fit with a spectral index $\gamma$ as

$$\Phi(e^+ + e^-) = CE^{\gamma} \quad \text{or} \quad \gamma = d[\log(\Phi)]/d[\log(E)] \qquad (3)$$

($E$ in GeV and $C$ is a normalization) over a sliding energy window. The width of the window varies with energy to have sufficient sensitivity to determine the spectral index. The resulting energy dependence of the fitted spectral index is shown in Fig. 4(a), where the shading indicates the

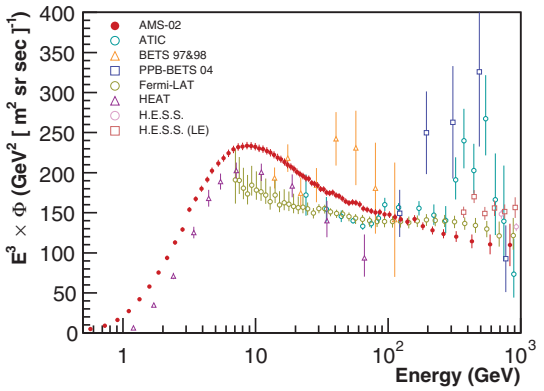


FIG. 3 (color). The flux of electrons plus positrons $\Phi(e^+ + e^-)$ measured by AMS multiplied by $\tilde{E}^3$ versus energy. The AMS error bars are the quadratic sum of the statistical and systematic errors. Also shown are the results from earlier experiments [11–17].

correlation between neighboring points due to the sliding energy window. Fitting a single power law over the range 30.2 GeV to 1 TeV yields $\gamma = -3.170 \pm 0.008 \pm 0.008$, where the first error is the combined statistical and systematic uncertainty and the second error is due to the energy scale uncertainty. This is shown in Fig. 4(b).

It is important to note, as discussed in Ref. [3], that a single power law can describe the electron flux above 52.3 GeV and a single power law, with a different spectral index, can describe the positron flux above 27.2 GeV. The simultaneous single power law behavior of $\Phi(e^+)$, $\Phi(e^-)$, and $\Phi(e^+ + e^-)$ is unexpected.

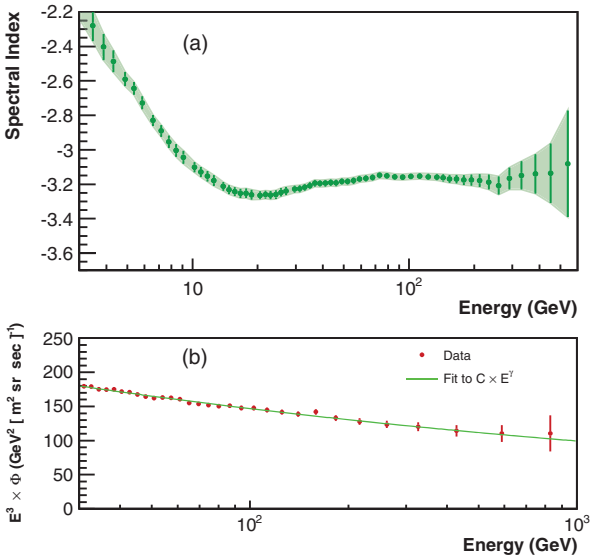


FIG. 4 (color). (a) The spectral index of $\Phi(e^+ + e^-)$ as a function of energy. The shaded regions indicate the 68% C.L. intervals including the correlation between neighboring points due to the sliding energy window. (b) $\Phi(e^+ + e^-)$ multiplied by $\tilde{E}^3$ versus energy and the result of a single power law fit above 30.2 GeV.

This measurement of $\Phi(e^+ + e^-)$ together with the measurements of $\Phi(e^+)$ and $\Phi(e^-)$ [3] and the positron fraction make possible the accurate comparison with various particle physics and astrophysics models including the minimal model discussed in Refs. [1,2]. This will be presented in a separate publication.

In conclusion, the precision measurement of $\Phi(e^+ + e^-)$ as a function of energy from 0.5 GeV to 1 TeV indicates that the flux is smooth and reveals new and distinct information. No structures were observed. From 30.2 GeV to 1 TeV, the flux can be described by a single power law with $\gamma = -3.170 \pm 0.008(\text{stat} + \text{syst}) \pm 0.008$ (energy scale).

We thank former NASA Administrator Daniel S. Goldin for his dedication to the legacy of the ISS as a scientific laboratory and his decision for NASA to fly AMS as a DOE payload. We also acknowledge the support of the NASA leadership including Charles Bolden and William Gerstenmeier. We are grateful for the support of Jim Siegrist and Michael Salamon of the DOE. We also acknowledge the continuous support from MIT and its School of Science, Michael Sipser, Marc Kastner, Ernest Moniz, and Richard Milner. Research supported by: CAS, NNSF, MOST, NLAA, the provincial governments of Shandong, Jiangsu, and Guangdong, and the China Scholarship Council, China, including work at IHEP by the National Natural Science Foundation; CNRS, IN2P3, CNES, Enigmass, and the ANR, France including support of M. Vecchi by CNES; J. Trümper, J.D. Woerner, and DLR, Germany, including work at Aachen University and KIT by the Deutsches Zentrum für Luft- und Raumfahrt and computing resources from JARA-HPC under Project No. JARA0052 for Aachen and Jülich; INFN and ASI, Italy, including the work of J. Bazo, F. Nozzili, and C. Pizzolotto at the ASI Science Data Center in the framework of ASI-INFN Agreement No. C/011/11/1 and work at INFN Sezioni di Bologna, Milano, Perugia, Pisa, Roma, and Trento by the Italian Space Agency (ASI), Contract No. ASI-INFN I/002/13/0; Grants No. NRF-2009-0080142 and No. NRF-2012-010226 at CHEP, Kyungpook National University and Grant No. NRF-2013-004883 at Ewha Womans University, Korea; the Consejo Nacional de Ciencia y Tecnologa at UNAM, Mexico; CIEMAT, CDTI, and, at CIEMAT, by SEIDI–MINECO, and CPAN, Spain; the Swiss National Science Foundation (SNSF), federal and cantonal authorities, Switzerland; Academia Sinica and the National Science Council (NSC), former President of Academia Sinica Yuan-Tseh Lee and former Ministers of NSC, Maw-Kuen Wu and Luo-Chuan Lee, Taiwan, including work at both NCU and the Institute of Physics, Academia Sinica, by the Ministry of Science and Technology; and the Turkish Atomic Energy Authority at METU, Turkey. We gratefully acknowledge the strong support from CERN, including Rolf-Dieter Heuer, and from the European Space Agency.

We are grateful for important discussions with Barry Barish, Jonathan Ellis, Jonathan Feng, Steve Olsen, George Smoot, Michael Turner, Steven Weinberg, and Frank Wilczek. The strong support of the JSC and MSFC flight control teams has allowed AMS to operate optimally on the ISS for over three years.

[*]Deceased.
[a]Currently at ISDC, CH–1290 Versoix, Switzerland.
[b]Also at ASI, I–00133 Roma, Italy.
[c]Also at Xi'an Jiaotong University (XJTU), Xi'an 710049, China.
[d]Also at Sun Yat–Sen University (SYSU), Guangzhou 510275, China.
[e]Currently at European Organization for Nuclear Research (CERN), CH–1211 Geneva 23, Switzerland.
[f]Also at Shandong University (SDU), Jinan, Shandong 250100, China.
[g]Also at Harbin Institute of Technology (HIT), Harbin 150001, China.
[h]Also at University of Science and Technology of China (USTC), Hefei 230026, China.
[i]Also at Università di Siena, I–53100 Siena, Italy.
[j]Also at Beijing Normal University (BNU), Beijing 100875, China.
[k]Also at Southeast University (SEU), Nanjing 210096, China.

[1] M. Aguilar *et al.*, Phys. Rev. Lett. **110**, 141102 (2013).
[2] L. Accardo *et al.*, Phys. Rev. Lett. **113**, 121101 (2014).
[3] M. Aguilar *et al.*, Phys. Rev. Lett. **113**, 121102 (2014).
[4] L. Feng R.-Z. Yang, H.-N. He, T.-K. Dong, Y.-Z. Fan, and J. Chang, Phys. Lett. B **728**, 250 (2014); K. Blum, B. Katz, and E. Waxman, Phys. Rev. Lett. **111**, 211101 (2013); L. Bergström, T. Bringmann, I. Cholis, D. Hooper, and C. Weniger, Phys. Rev. Lett. **111**, 171101 (2013); I. Cholis and D. Hooper, Phys. Rev. D **88**, 023013 (2013); T. Linden and S. Profumo, Astrophys. J. **772**, 18 (2013); R. Cowsik, B. Burch, and T. Madziwa-Nussinov, Astrophys. J. **786**, 124 (2014).
[5] A. Kounine, Int. J. Mod. Phys. E **21**, 1230005 (2012); S. Rosier-Lees, in *Proceedings of Astroparticle Physics TEVPA/IDM*, Amsterdam, 2014 (to be published); S. C. C. Ting, Nucl. Phys. B, Proc. Suppl. **243–244**, 12 (2013); S.-C. Lee, in *Proceedings of the 20th International Conference on Supersymmetry and Unification of Fundamental Interactions (SUSY 2012)*, Beijing, 2012 (unpublished); M. Aguilar, in *Proceedings of the XL International Meeting on Fundamental Physics*, Centro de Ciencias de Benasque Pedro Pascual, 2012 (unpublished); S. Schael, in *Proceedings of the 10th Symposium on Sources and Detection of Dark Matter and Dark Energy in the Universe*, Los Angeles, 2012 (unpublished); B. Bertucci, Proc. Sci., EPS-HEP (2011) 67; M. Incagli, AIP Conf. Proc. **1223**, 43 (2009); R. Battiston, Nucl. Instrum. Methods Phys. Res., Sect. A **588**, 227 (2008).
[6] B. P. Roe, H.-J. Yang, J. Zhu, Y. Liu, I. Stancu, and G. McGregor, Nucl. Instrum. Methods Phys. Res., Sect. A **543**, 577 (2005).
[7] J. Allison *et al.*, IEEE Trans. Nucl. Sci. **53**, 270 (2006); S. Agostinelli *et al.*, Nucl. Instrum. Methods Phys. Res., Sect. A **506**, 250 (2003).
[8] J. Alcaraz *et al.*, Phys. Lett. B **484**, 10 (2000).
[9] D. Smart and M. Shea, Adv. Space Res. **36**, 2012 (2005); C. Størmer, *The Polar Aurora* (Oxford University Press, London, 1950).
[10] G. D. Lafferty and T. R. Wyatt, Nucl. Instrum. Methods Phys. Res., Sect. A **355**, 541 (1995). We have used Eq. (6) with $\tilde{\boldsymbol{E}} \equiv \boldsymbol{x}_{lw}$.
[11] S. Torii *et al.*, Astrophys. J. **559**, 973 (2001).
[12] M. A. DuVernois *et al.*, Astrophys. J. **559**, 296 (2001).
[13] J. Chang *et al.*, Nature (London) **456**, 362 (2008).
[14] K. Yoshida *et al.*, Adv. Space Res. **42**, 1670 (2008).
[15] F. Aharonian *et al.*, Phys. Rev. Lett. **101**, 261104 (2008).
[16] F. Aharonian *et al.*, Astron. Astrophys. **508**, 561 (2009).
[17] M. Ackermann *et al.*, Phys. Rev. D **82**, 092004 (2010).